Diffuse correlation spectroscopy measurements of blood flow using 1064 nm light

**Stefan A. Carp,[a,]* Davide Tamborini,[a] Dibbyan Mazumder,[a]
Kuan-Cheng (Tony) Wu,[a,b] Mitchell R. Robinson,[a,c]
Kimberly A. Stephens,[a] Oleg Shatrovoy,[d] Niyom Lue,[d] Nisan Ozana,[a]
Megan H. Blackwell,[d] and Maria A. Franceschini[a]**

[a]Massachusetts General Hospital, Harvard Medical School, Optics at Athinoula A. Martinos Center for Biomedical Imaging, Department of Radiology, Charlestown, Massachusetts, United States
[b]Boston University, Department of Biomedical Engineering, Boston, Massachusetts, United States
[c]MIT, Health Sciences and Technology Program, Cambridge, Massachusetts, United States
[d]MIT Lincoln Laboratory, Lexington, Massachusetts, United States

Abstract

Significance: Diffuse correlation spectroscopy (DCS) is an established optical modality that enables noninvasive measurements of blood flow in deep tissue by quantifying the temporal light intensity fluctuations generated by dynamic scattering of moving red blood cells. Compared with near-infrared spectroscopy, DCS is hampered by a limited signal-to-noise ratio (SNR) due to the need to use small detection apertures to preserve speckle contrast. However, DCS is a dynamic light scattering technique and does not rely on hemoglobin contrast; thus, there are significant SNR advantages to using longer wavelengths (>1000 nm) for the DCS measurement due to a variety of biophysical and regulatory factors.

Aim: We offer a quantitative assessment of the benefits and challenges of operating DCS at 1064 nm versus the typical 765 to 850 nm wavelength through simulations and experimental demonstrations.

Approach: We evaluate the photon budget, depth sensitivity, and SNR for detecting blood flow changes using numerical simulations. We discuss continuous wave (CW) and time-domain (TD) DCS hardware considerations for 1064 nm operation. We report proof-of-concept measurements in tissue-like phantoms and healthy adult volunteers.

Results: DCS at 1064 nm offers higher intrinsic sensitivity to deep tissue compared with DCS measurements at the typically used wavelength range (765 to 850 nm) due to increased photon counts and a slower autocorrelation decay. These advantages are explored using simulations and are demonstrated using phantom and *in vivo* measurements. We show the first high-speed (cardiac pulsation-resolved), high-SNR measurements at large source–detector separation (3 cm) for CW-DCS and late temporal gates (1 ns) for TD-DCS.

Conclusions: DCS at 1064 nm offers a leap forward in the ability to monitor deep tissue blood flow and could be especially useful in increasing the reliability of cerebral blood flow monitoring in adults.

*Address all correspondence to Stefan A. Carp, E-mail: stefan.carp@mgh.harvard.edu

1 Introduction

Diffuse optical methods have been used for more than 30 years to noninvasively quantify hemodynamics in the brain, skeletal muscles, and other tissues. In particular, near-infrared spectroscopy (NIRS) is widely adopted for cerebral oximetry clinical applications[1] and functional neuroimaging studies.[2] NIRS employs light in the red and near-infrared spectral region, between 650 and 900 nm, where overall tissue absorption is low and dominated by hemoglobin species while water absorption is not significant. This optical window permits light penetration of several centimeters into the tissue and high sensitivity to hemoglobin concentration changes. Diffuse correlation spectroscopy (DCS)[3,4] is another diffuse optical method that is rapidly growing and being employed in a range of biomedical applications.[5–7] In DCS, a tissue of interest is illuminated by coherent near-infrared light, which causes a speckled interference pattern to form after the light scatters multiple times through the tissue. Dynamic scattering of the light by moving red blood cells causes the speckle pattern to fluctuate rapidly. These fluctuations are typically detected 2 to 3 cm away from the source and are quantified by measuring the temporal intensity autocorrelation curve, $g_2(\tau) = \langle I(t)I(t + \tau)\rangle / \langle I(\tau)\rangle^2$, of a single speckle. The decay of the autocorrelation curve is fit with the solution of the correlation diffusion equation[4] to obtain an index of blood flow (BF$_i$) in units of cm^2/s. Although the units of BF$_i$ are not the conventional units of ml/min/100 g tissue for perfusion, BF$_i$ has been shown to be reliably proportional to absolute flow, as demonstrated against "gold standards," such as arterial spin-labeled MRI,[8–10] fluorescent microspheres,[11] bolus tracking time-domain NIRS,[12,13] and phase-encoded velocity mapping MRI.[14]

A significant limitation of both NIRS and DCS is the limited depth sensitivity, which is crucial when aiming to measure cerebral hemodynamics noninvasively in humans. NIRS cerebral oximetry measurements of hemoglobin oxygenation (SO$_2$) are contaminated by scalp and skull physiology, and the resulting SO$_2$ includes extracranial contributions.[15–18] This uncertainty on the cerebral origin of the signal limits the widespread adoption of NIRS cerebral oximeters in the clinical practice.[19,20] Similarly, in functional NIRS imaging studies, the low-depth sensitivity not only limits the method of studying the superficial cortical regions but also reduces the contrast of the measured evoked hemodynamic changes. DCS is more sensitive to faster flow, and blood flow in the brain is usually 4 to 6 times higher than scalp blood flow,[21] which should make DCS more sensitive to brain hemodynamics than NIRS.[22] However, this would hold true only if the signal-to-noise ratio (SNR) of the two modalities were comparable.

In this paper, we demonstrate that SNR strongly impacts effective DCS depth sensitivity and, through the use of longer wavelengths than what has conventionally been used in NIRS, show how we can substantially improve DCS SNR and hence sensitivity to deep tissue blood flow. The use of longer wavelengths to increase light penetration[23] has already been applied in the microscopic imaging domain by modalities such as multiphoton microscopy,[24,25] optical coherence tomography,[26] and photoacoustic imaging.[27] Here we show theoretically and experimentally the advantages of operating DCS at 1064 nm, we highlight current hardware component limitations, and we report initial feasibility of DCS measurements in humans at this wavelength, comparing performances with DCS in the typical NIRS wavelength range. In particular, we demonstrate for the first time the ability to make high-speed cardiac pulsation-resolved measurements with high-deep-tissue sensitivity, achieved through large (3 cm) source–detector separations for continuous wave DCS and late temporal gates (1 ns start time) for time-domain DCS.

2 Theoretical Advantages of DCS at 1064 nm versus 765 to 850 nm

2.1 Light Attenuation Coefficient and Depth Penetration

Absorption in biological tissues is dominated by hemoglobin in the ultraviolet and visible spectral regions (200 to 650 nm) and by water for wavelengths above 900 nm.[28] Between 650 and 900 nm, absorption is more than one order of magnitude lower, and NIRS uses this transmission window to investigate tissue several cm below the surface. Between 1050 and 1100 nm, the water spectrum has a local minimum [Fig. 1(a)], offering an additional transmission window for deep tissue measurements. Above 1100 nm, water absorption continues to increase with peaks and
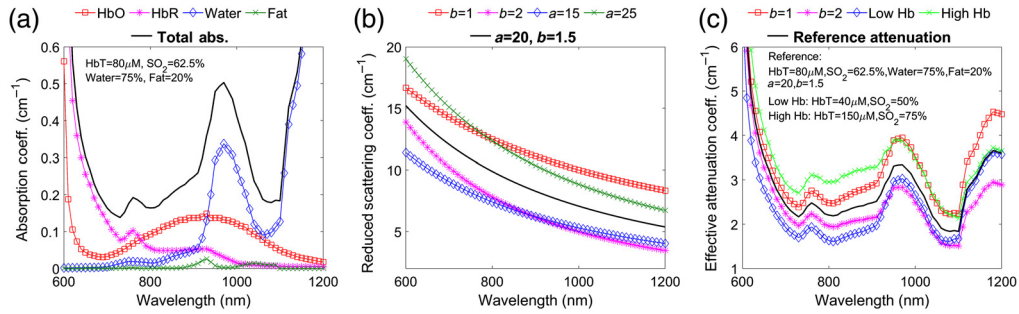
Fig. 1 (a) Absorption spectra of main chromophores in brain tissue between 600 and 1200 nm assuming HbT = 80 μM, SO$_2$ = 62.5%, 20% volume fraction of fat and 75% volume fraction of water: oxy-hemoglobin (HbO), red squares; deoxy-hemoglobin (HbR), magenta stars; water, blue diamonds; and fat, green crosses. The thick black line is the resulting total absorption. Absorption of melanin, cytochrome oxidase, and other possible chromophores is below 10^{-3} cm^{-1} in most biological tissues. For shorter wavelengths, hemoglobin absorption increases; for longer wavelengths, water absorption further increases. (b) Reduced scattering coefficient assuming a power law wavelength dependence with $a = 20$ and $b = 1.5$ for $\lambda_0 = 500$ nm, thick black line, and changing a and b within physiological ranges, colored lines with symbols. (c) Resulting effective attenuation coefficient: thick black line attenuation is derived from the total absorption of (a) and reduced scattering coefficient with $a = 20$ and $b = 1.5$ for $\lambda_0 = 500$ nm; for red squares and magenta stars, we assumed $b = 1$ and 2, respectively; blue diamonds for low hemoglobin, assuming HbT = 40 μM and SO$_2$ = 50%; green crosses for high hemoglobin, assuming HbT = 150 μM and SO$_2$ = 75%.

minima well above the 1050 to 1100 nm values. Figure 1(a) shows the absorption spectra of the main tissue chromophores between 600 and 1200 nm using assumptions typical for the brain. For the hemoglobin absorption, we assumed a concentration (HbT) of 80 μM, an oxygenation (SO$_2$) of 62.5%, and used extinction coefficients compiled by Prahl et al.[29] as well as by Bosschaart et al.[30] For the water absorption, we used values from Hale et al.[31] and assumed a 75% volume fraction in tissue.[32] For fat absorption, we used values from van Veen et al.[33] and assumed a 20% volume fraction.[34] Under these assumptions, the total absorption coefficients (μ_a) at 765, 785, and 850 nm, wavelengths commonly used for DCS, are 0.19, 0.17, and 0.20 cm^{-1}, respectively, very similar to the total absorption at 1064 nm (0.18 cm^{-1}). By varying the hemoglobin concentration between 40 and 120 μM, hemoglobin oxygenation between 40% and 95%, fat content between 0% and 40%, and water content between 55% and 95%, on average, we obtain absorption coefficients equal to the one in our example (see Table 1).

In biological tissues, the reduced scattering coefficient (μ_s') decreases with wavelength and follows the empirical power law relationship of $\mu_s'(\lambda) = a(\lambda/\lambda_0)^{-b}$, where a is a scaling factor at wavelength λ_0 and b is the scattering power. The scattering spectra for typical values of $a = 20$ at $\lambda_0 = 500$ nm and $b = 1.5$ (black line)[28,33] are shown in Fig. 1(b), together with additional example spectra assuming $a = 15$, $a = 25$, $b = 1$, or $b = 2$. Similarly, we varied the scattering

Table 1 Mean and standard deviation of optical properties across the range of chromophore concentrations considered in simulation.

λ (nm)	μ_a (cm^{-1})	μ_s' (cm^{-1})	μ_{eff} (cm^{-1})
765	0.19 ± 0.08	9.2 ± 3.3	2.2 ± 0.8
785	0.17 ± 0.07	8.8 ± 3.2	2.1 ± 0.7
850	0.20 ± 0.08	8.0 ± 3.0	2.1 ± 0.7
1064	0.18 ± 0.04	6.0 ± 2.4	1.7 ± 0.5

parameters over a wide range of $8 < a < 25$ and $0.5 < b < 2.4$ and calculated that on average at 1064 nm μ'_s is 35%, 32%, and 25% lower than at 765, 785, and 850 nm, respectively (Table 1).

The cumulative effect of absorption and scattering on light propagation in the diffusive regime is given by the effective attenuation coefficient [$\mu_{\mathrm{eff}}(\lambda) = \sqrt{3\mu_a(\mu_a + \mu'_s)}$]. Figure 1(c) reports μ_{eff} spectra for typical absorption and scattering [black lines in (a)–(c)], for high- and low-scattering power ($b = 1$ red squares and $b = 2$ magenta stars), and for low and high hemoglobin concentration (40 μM: blue diamonds and 150 μM: green crosses). Over the wide ranges of absorption and scattering described above, the average effective attenuation coefficient for diffuse light at 1064 nm is 23%, 21%, and 21% lower than at 765, 785, and 850 nm, respectively (Table 1).

In the examples of Fig. 1, we used a high content of water (75%), typical of brain tissue.[32] For biological tissues with lower water content, the reduction in the effective attenuation at 1064 nm is even larger, despite the increase in fat content, which has a negligible contribution.

Figure 2 presents histograms of the optical absorption, reduced scattering, and effective attenuation coefficients at 765, 785, 850, and 1064 nm, respectively, across 150,000 randomly sampled scenarios from the tissue chromophore concentration and scattering parameter ranges given above. Of note, when compared in a pairwise fashion across wavelengths for each randomly chosen chromophore concentration and scattering parameter choice set, the effective attenuation coefficient was lower at 1064 nm than at 765, 785, and 850 nm in 96%, 93%, and 99% of the time, respectively.

A lower effective attenuation coefficient implies a larger number of photons traveling through the tissue will be able to reach the detector. In fact, in the diffusive regime, the relationship between the detected intensity at two wavelengths is
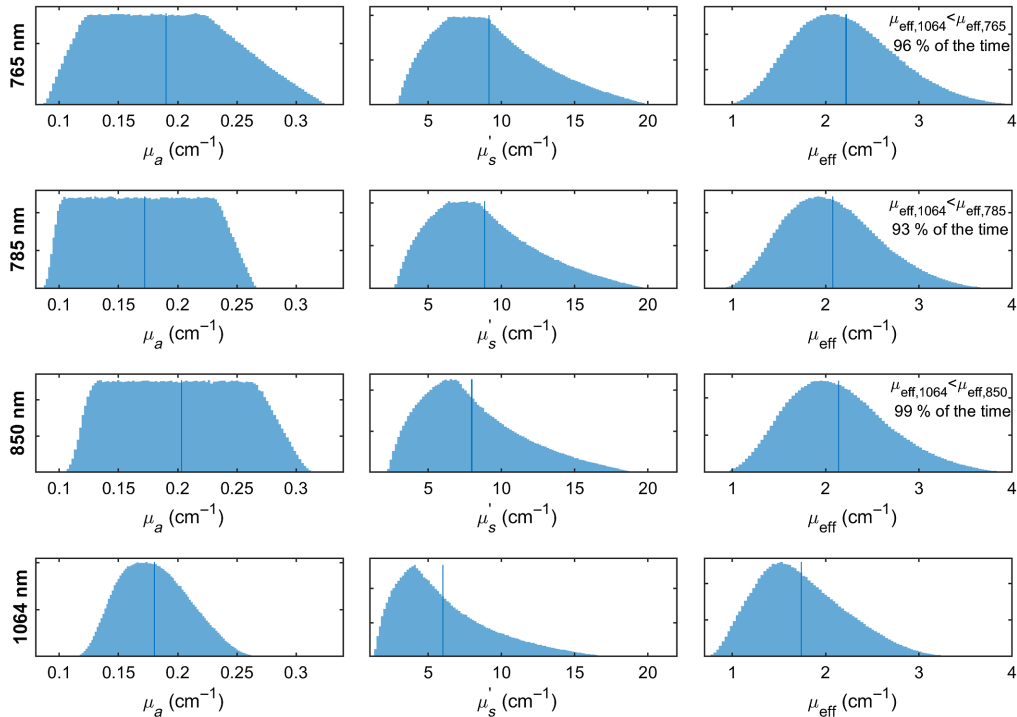
Fig. 2 Histograms of absorption, reduced scattering, and effective attenuation coefficients at 765, 785, 850, and 1064 nm, respectively, randomly sampled ($N = 150{,}000$) for 40 μM < HbT < 120 μM, 40% < SO_2 < 85%, 0.55 < f_{H2O} < 0.95, 0 < f_{fat} < 0.4, 8 < a < 25, 0.5 < b < 2.4 to cover the vast majority of possible circumstances for tissue measurements. Vertical bars indicate average values. In pairwise comparisons (across the set of randomly sampled parameters), $\mu_{\mathrm{eff},1064}$ was lower than $\mu_{\mathrm{eff},765}$, $\mu_{\mathrm{eff},785}$, and $\mu_{\mathrm{eff},850}$ in 96%, 93%, and 99% of the time, respectively, indicating 1064 nm nearly always offers lower attenuation than the shorter wavelengths commonly used for DCS measurements.

$$I_{\lambda_2}/I_{\lambda_1} = e^{\left(\frac{\mu_{\text{eff}_{\lambda_1}} - \mu_{\text{eff}_{\lambda_2}}}{\mu_{\text{eff}_{\lambda_1}}}\right) \cdot r},$$

and for $r = 3$ cm, μ_{eff} (765 nm) $= 2.2 \pm 0.8$ cm^{-1}, μ_{eff} (785 nm) $= 2.1 \pm 0.7$ cm^{-1}, μ_{eff} (850 nm) $= 2.1 \pm 0.7$ cm^{-1}, and μ_{eff} (1064 nm) $= 1.7 \pm 0.5$ cm^{-1}, the number of photons available at the detector at 1064 nm is, on average, 1.7 to 2.0 times larger than at wavelengths between 765 and 850 nm. Further, the lower attenuation results in longer (thus deeper) photon pathlengths being detectable, extending the penetration depth of the DCS measurement.

The fact that hemoglobin absorption is low at 1064 nm makes this wavelength choice impractical for NIRS, but this is not an issue for DCS as DCS contrast arises from the dynamic scattering of light by moving red blood cells, which is still high at 1064 nm. The lower scattering at 1064 nm does result in a somewhat reduced sensitivity to motion; however, this is more than compensated for by the other favorable aspects of using 1064 nm operation, as demonstrated below.

2.2 Overall Photon Budget Considerations

In addition to the lower attenuation, other factors contribute to the larger number of detectable photons at 1064 nm than at conventional DCS wavelengths.

DCS, like NIRS, needs to be performed in compliance with the ANSI standards limits for safe skin exposure (ANSI Z136.1) to be categorized as a nonsignificant risk device; thus, it needs to irradiate the tissue with low-power light. Based on these standards, the maximum permissible exposure (MPE) of skin by optical illumination are MPE$_{765} = 0.27$ W/cm^2, MPE$_{785} = 0.29$ W/cm^2, MPE$_{850} = 0.40$ W/cm^2, while from 1000 to 1400 nm MPE$_{1000-1400} = 1.07$ W/cm^2. Per the standard, for an illumination spot larger than 1-mm-diameter, a 3.5-mm aperture can be applied, translating to a light power of 26 mW at 765 nm, 28 mW at 785 nm, 38 mW at 850 nm, and 103 mW at 1064 nm. This means that at 1064 nm we can deliver 2.7 to 4 times more energy than at wavelengths between 765 and 850 nm. Moreover, because photons at longer wavelengths carry less energy $E_{\lambda_2} = E_{\lambda_1} \cdot \frac{\lambda_1}{\lambda_2}$, at longer wavelengths this increases the number of photons per unit of energy. Hence at 1064 nm, we can emit 1.3 to 1.4 times more photons per unit of illumination power than at wavelengths between 765 and 850 nm.

Multiplying together these three factors, i.e., the lower effective attenuation, the higher MPE, and the larger number of photons per unit of energy, using a 3-cm source–detector separation at 1064 nm, we end up with 13, 10.5, and 7 times more photons at the detector than at 765, 785, and 850 nm, respectively. This is a considerable gain as the number of photons directly impacts the measurement SNR.

2.3 Intensity Autocorrelation Noise Considerations

Figure 3(a) shows example g_2 curves for a 3-cm source–detector separation, using the optical properties in Table 1 and assuming a blood flow index, BF$_i = 2 \times 10^{-8}$ cm^2/s. The lower scattering and longer wavelength result in a later autocorrelation decay at 1064 nm versus shorter wavelengths, moving the correlation transition region to longer delay time bins where the statistical fluctuation noise is lower at a given photon count. Figure 3(b) shows updated g_2 simulations in which all factors discussed so far are taken into account to generate curves with realistic noise based on the DCS correlation noise model from Zhou.[35] To this end actual photon counts needed to be specified, which in fact is one of the major advantages of operating at 1064 nm. Hence, we assumed a photon count rate of 7 kcps through a single-mode fiber for the 765-nm measurement, estimated from our experience with in vivo measurements. We simulated measuring with four co-located detector fibers to increase SNR[36]—as is often done in practice. This photon count rate was scaled up conservatively by just half of the factors estimated in Sec. 2.2 at the other wavelengths and considered 8050 counts per second at 785 nm, 10,900 counts per second at 850 nm, and 42,500 counts per second at 1064 nm. A 10-s averaging time was assumed. It is apparent from this simulation that, even under these conservative assumptions, 1064 nm measurements benefit from a substantial increase in SNR.

(a) **Simulated g_2 curves** (b) **Simulated g_2 curves w/ realistic noise**
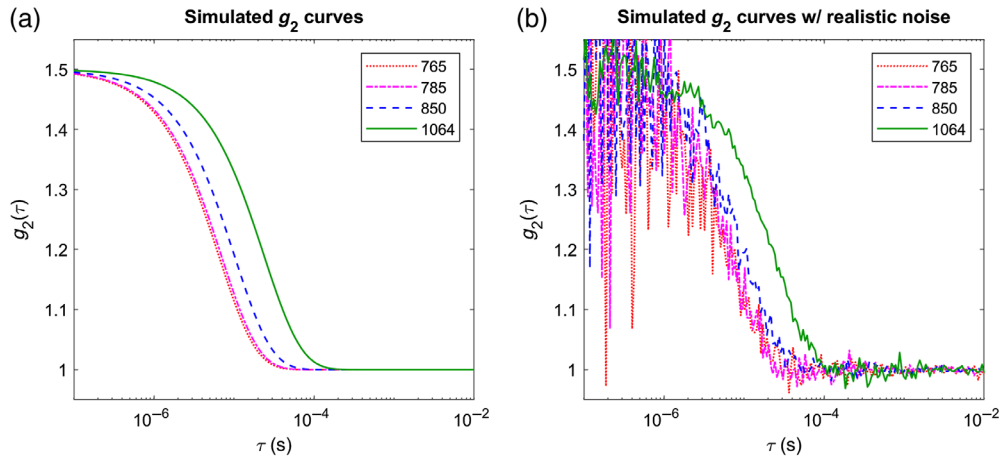
Fig. 3 Simulated g_2 curves for measurements with 3-cm source–detector separation on a homogeneous sample with optical properties matching Table 1, assuming $\beta = 0.5$, an integration time of 10 s, and a blood flow index $BF_i = 2 \times 10^{-8}$ cm^2/s: (a) noise free; (b) with realistic noise added assuming a 7-kcps count rate at 765 nm, 8.05 kcps at 785 nm, 10.9 kcps at 850 nm, and 42.5 kcps 1064 nm on each of 4 co-located fibers.

2.4 Monte Carlo Simulations of Sensitivity to Deep Blood Flow Change in the Presence of Realistic Noise

To further give a realistic assessment of the expected performance of DCS at 1064 nm in practice, we used Monte Carlo simulations in conjunction with a correlation noise model[35] and typical experimental parameters to estimate the level of change in cerebral blood flow that can be detected with 95% confidence and 80% power. To this end, we considered a two-layered slab, with a superficial layer thickness of 1 cm and ran separate simulations corresponding to 765, 850, and 1064 nm illumination, respectively. For the two layers, we assumed typical hemoglobin and water concentrations as reported in the literature.[37] Specifically, we assumed that the superficial layer contains 30 μM HbT, with a 66% SO$_2$ and has a water fraction of 0.6. We assumed that the deep (cerebral) layer contains 80 μM HbT with a 62.5% SO$_2$ and has a water fraction of 0.75 (as in Fig. 1). Optical absorption was derived from these chromophore concentrations using published extinction coefficients at each wavelength as detailed in the previous sections. Optical scattering was assumed to be homogeneous, equal to 9, 8, and 6 cm^{-1}, respectively, at the three wavelengths, following the average optical scattering derived in the previous section (as shown in Table 1). A blood flow index of 1×10^{-8} cm^2/s was assumed for the superficial layer, and a blood flow index of 6×10^{-8} cm^2/s was assumed for the deep layer, similar to our previous publication.[22] To assess sensitivity to changes in blood flow in the deeper layer, the deep flow was increased in turn by amounts from 1% to 100% in steps of 1%. We fixed the source–detector separation to 3 cm, the largest source–detector separation commonly used for *in vivo* measurements with existing DCS systems.

Electric field autocorrelation functions $g_1 = \langle E(t)E^*(t+\tau)\rangle/\langle E(t)E^*(t)\rangle$ were derived from photon pathlengths and momentum transfer accumulations in each tissue type using the MCX simulation package.[38] g_1 curves were then converted to intensity autocorrelation g_2 curves using the Siegert relationship $g_2 = 1 + \beta \cdot g_1^2$ with $\beta = 0.5$ corresponding to polarization-insensitive detection.

The Monte Carlo generated g_2 curves were further modified to add realistic noise levels based on the model of Zhou.[35] Hence, taking into account the photon budget considerations discussed in Sec. 2.2, we used the same fluence values as used in Sec. 2.3 and assumed four co-located fibers as well. The noise model predicted standard deviations for g_2 at each lag time were applied by randomly sampling a normal distribution. A total of 60 noise realizations were obtained at each flow level, and the integration time in the noise model was set to 1 s, i.e., we simulated 60 1-s measurements at each flow level.
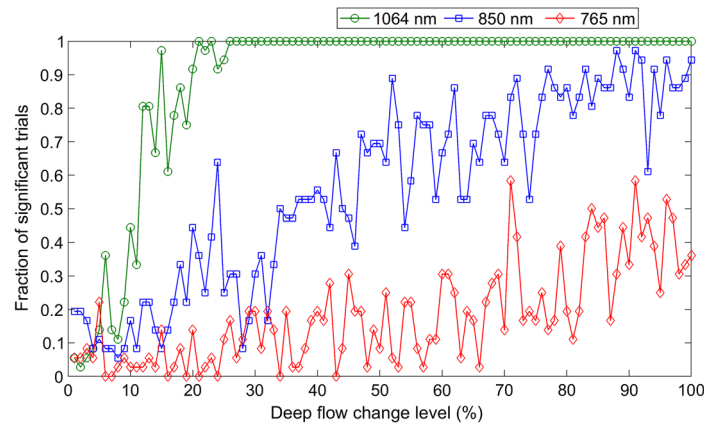
Fig. 4 Probability of detecting a statistically significant change in deep-tissue blood flow from a pair of 10 s measurements as a function of the actual amount of change for noise-realistic simulated measurements at 765 nm (red diamonds), 850 nm (blue squares), and 1064 nm (green circles). We assumed 30 μM HbT, with a 66% SO$_2$, water fraction of 0.6 (no fat), and BF$_i$ = 10^{-8} cm^2/s for the superficial layer (1-cm thick), and 80 μM HbT with a 62.5% SO$_2$, water fraction of 0.75 (also with no fat), and BF$_i$ = 6×10^{-8} cm^2/s for the deep layer. The source–detector separation was set to 3 cm, and we assumed 7 kcps at 765 nm on four co-located fibers, scaling up to 10.9 and 42.5 kcps at 850 and 1064 nm, respectively, reflecting conservative estimates of the benefits of longer wavelengths.

To generate population-based statistics, each sequence of 60 "measurements" (at baseline or at elevated deep flow levels, respectively) was divided into six 10-s segments. Each baseline segment was combined with each elevated flow segment at each flow level providing a population of 36 "trials" at each deep flow change level. Thus each trial was an attempt to detect a statistically significant change ($p < 0.05$) in deep flow by comparing 10 s of baseline data with 10 s of elevated flow data, both acquired with a 1-s integration time. We consider this to be a realistic scenario for neuromonitoring in clinical practice, for example.

Figure 4 shows the results of the simulations. DCS at 765 nm (red diamonds) is able to detect significant changes in blood flow in, at best, 30% to 40% of the trials even for the highest level of simulated deep blood flow changes (above 80% with respect to baseline). DCS at 850 nm (blue squares) performances are somewhat better, though deep flow changes above 75% are needed to achieve an 80% detection rate of deep flow change. By comparison, the performance of DCS at 1064 nm (green circles) is dramatically better with more than 80% of the trials able to detect a statistically significant change in deep blood flow of 20% or more.

3 Experimental Demonstration of DCS at 1064 nm and Comparison with DCS at 765 to 850 nm

3.1 DCS Hardware at 1064 nm

3.1.1 CW-DCS system

For our measurements, we used a custom-built multicolor DCS system[39] built in house and replaced one of the sources with a laser at 1064 nm. Specifically, we kept the monolithic distributed Bragg reflector (DBR) lasers at 765 and 850 nm (PH765DBR and PH850DBR by Photodigm Inc.) and replaced the laser at 808 nm with a DBR laser emitting at 1064 nm (PH1064DBR). The same custom circuitry was used to drive this laser, without fast multiplexing between the three lasers, allowing for operation at a wavelength manually selected each time. Later experiments used a 785-nm laser from CrystaLaser due to a hardware issue with the 765-nm Photodigm device. For the detectors, this system uses a single-photon avalanche diode (SPCM-850-14-FC, by Excelitas Technologies), which has a good photon detection efficiency (PDE) at 765 and 850 nm (64% and 54%, respectively) but only 3% efficiency at 1064 nm.

The low PDE of the silicon detectors at 1064 was a limiting factor on the choice of source–detector separation and was taken into account when comparing performances at different wavelengths.

An alternative configuration used a TOPTICA eagleyard distributed feedback EYP-DFB-1064 laser diode as a source, amplified using a Cybel MantaRay fiber amplifier. The detectors in this case were either Photon Spot or Quantum Opus superconducting nanowire single-photon detectors (SNSPDs) with greater than 90% PDE at 1064 nm, the output from which was patched into our DCS system's correlator board. The use of SNSPDs was necessitated by the shortcomings of commercially available InGaAs SPADs that have unacceptably long afterpulsing, which prevents the effective measurement of the autocorrelation decay at longer source–detector separations needed to be sensitive to brain blood flow.

3.1.2 *TD-DCS system*

To acquire proof-of-concept data using time-domain diffuse correlation spectroscopy (TD-DCS) at 1064 nm, we modified our previously reported portable TD-DCS system[40] to replace the source and detection components, while reusing the time-tagging and correlation hardware. We used a 1064-nm Picoquant seed laser emitting ∼650 ps FWHM pulses with a repetition rate of 80 MHz at an average power of about 5 mW. The output of the seed laser was coupled into a Cybel MantaRay fiber amplifier. The same Photon Spot or Quantum Opus SNSPD detector described above was used to capture the light returned from tissue.

3.2 *Phantom Measurements*

Figure 5 shows the CW-DCS temporal autocorrelation functions for 3-cm source–detector separation measured at 765 nm (red diamonds) and 1064 nm (green circles) in (a) silicone oil and (b) intralipid. The decay of g_2 is much slower (occurs at later time lags) for the two homogeneous liquid phantoms at 1064 nm because of the lower scattering and higher wavelength. If we calculate BF_i assuming reduced scattering values of 8 cm^{-1} at 765 nm and 6 cm^{-1} at 1064 nm, we obtain the same BF_i in the two phantoms.

Another set of liquid phantom titrations was used to further verify that the same dynamic properties are recovered no matter what wavelength is used to perform the measurements. The phantoms were constructed by adding India ink to a diluted intralipid suspension in water. Optical properties at 765 and 850 nm were measured using a frequency-domain NIRS device (ISS MetaOx). Optical properties at 1064 nm were extrapolated from measurements in the 660- to 830-nm range. As shown in Fig. 6, using CW-DCS at the three wavelengths, we were able to obtain agreement of 10% or better in the measured Brownian diffusion coefficient values across wavelengths when taking into account the actual optical properties. Of note, due to water
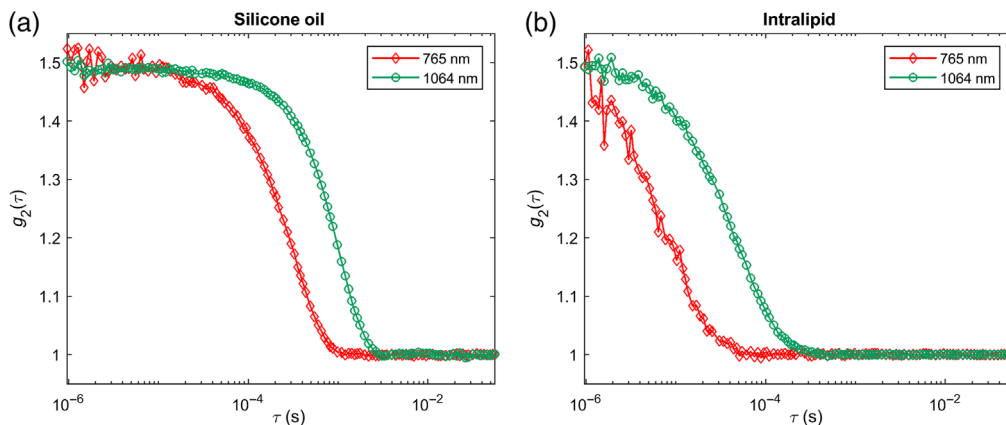
Fig. 5 Intensity autocorrelation function (g_2) measurements at 765 nm (red diamonds) and 1064 nm (green circles) in (a) a silicone oil phantom and (b) an intralipid phantom.
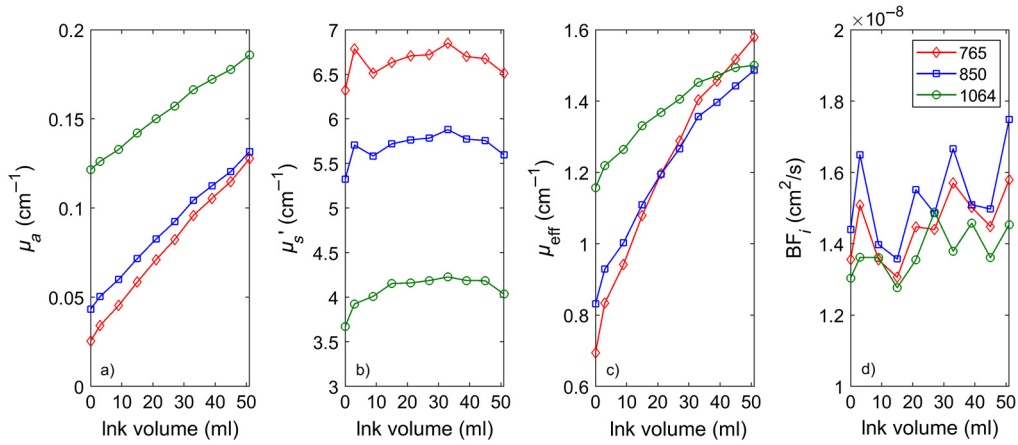
Fig. 6 CW-DCS measurements of BF$_i$ (in this case, the Brownian diffusion coefficient D_b) in a liquid phantom across wavelengths and phantom optical properties. (a) Optical absorption values, (b) corresponding optical scattering values, (c) corresponding attenuation coefficient values, and (d) recovered BF$_i$ taking into account actual optical properties.

absorption, significant amounts of ink needed to be added to obtain comparable absorption at 765 and 850 nm compared with 1064 nm.

3.3 In Vivo *Measurements*

We conducted several proof-of-concept experiments to demonstrate the feasibility of *in vivo* DCS data acquisition at 1064 nm and to exemplify the advantages of operating at this wavelength. Subject consent was obtained in accordance with the policies and guidelines of the Massachusetts General Hospital/Partners Healthcare Institutional Review Board.

3.3.1 *Muscle blood flow during arm cuff occlusion*

As a first demonstration, we conducted an arm cuff occlusion measurement on three healthy volunteers using both 765 nm and 1064 nm CW-DCS systems. These tests were conducted using the Excelitas SPADs; thus, we chose a 1-cm source–detector separation to compensate for the low PDE at 1064 nm. Figure 7 shows the time courses of the relative changes in blood flow index measured at 765 and 1064 nm, normalized to the average of the first 20 s for the three different subjects. After 40 s of baseline, the blood pressure cuff was quickly inflated to 160 mmHg in each case. The pressure was then released about 55 s later. Two measurements were conducted in succession on each subject at 765 and 1064 nm, respectively. Scattering values of 8 cm^{-1} at 765 nm and 6 cm^{-1} at 1064 nm were chosen to obtain matching absolute blood flow index
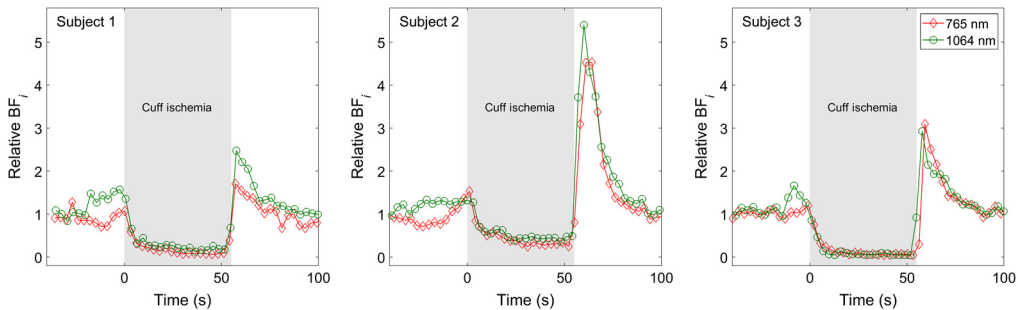
Fig. 7 Measurements of muscle blood flow before, during, and after an arm cuff occlusion maneuver in three different subjects. Measurements at 765 nm (red diamonds) and 1064 nm (green circles) were conducted one after the other. Despite the nonsimultaneous nature of the measurement, there is very good agreement between measurements taken in the same subject.

values at the baseline. Although the degree of blood flow reduction during occlusion and of reactive hyperemia when the pressure was released varied by subject, the DCS measurements at the two wavelengths agreed very well with each other, despite being conducted sequentially.

3.3.2 *Cerebral blood flow measurements*

Measurements were obtained using both the CW-DCS and TD-DCS systems on the forehead of an adult volunteer. The 765-nm (or 785 nm) measurements used our standard systems,[39,40] and we delivered 26 mW (28 mW at 785 nm) of average power on the skin surface. The 1064-nm measurements were conducted using the TOPTICA eagleyard single-frequency laser diode for CW-DCS and the Picoquant pulsed seed laser for TD-DCS, both amplified to 90 mW of average power using the Cybel MantaRay fiber amplifier. Either Photon Spot or Quantum Opus SNSPD detectors were used for both the CW-DCS and TD-DCS measurements at 1064 nm.

Figure 8 shows the CW-DCS temporal autocorrelation functions for a 3-cm source–detector separation measured at 765 nm (red diamonds) and 1064 nm (green circles) on an adult human forehead. The difference between the g_2s at the two wavelengths is smaller than in the phantom measurements shown in Fig. 5 (though remaining in favor of the 1064-nm measurement) because at 1064 nm light penetrates deeper and sees more of the brain blood flow. The higher sensitivity to the high perfusion in the brain "accelerates" the 1064-nm g_2, resulting in a more similar decay of g_2 at the two wavelengths. The 1064-nm measurement retains a significant SNR advantage due to the higher photon count ($\sim$55 kcps at 1064 nm versus 7 kcps at 765 nm in this case, driven by higher photon availability and higher PDE of the SNSPD detector even with more brain tissue in the photon path). If we calculate BF_i assuming values of 8 cm^{-1} at 765 nm and 6 cm^{-1} at 1064 nm, we obtain a BF_i that is 50% higher at 1064 nm than at 765 nm in the forehead.

Figure 9 shows the time course of CW-DCS BF_i at a 10-Hz acquisition rate, during a probe pressure modulation maneuver (marked by the gray shading starting just after the 60-s mark). By lightly pressing the optical probe onto the forehead, we reduce the blood flow to the skin under the probe. This results in a lower BF_i in the scalp and an unaffected BF_i in the brain. At a short source–detector separation (5 mm, orange/light green curves with open circles, respectively), we only measure BF_i in the scalp and the pressure modulation decreases BF_i substantially. At the same time, pulsatility is largely reduced. At a 3-cm separation (red/dark green curves with filled circles, respectively), we see a smaller reduction in average flow and pulsatility is preserved. Although evidence of cardiac cycle BF_i variation is visible at both wavelengths, the SNR of the 785-nm measurement is insufficient to resolve the pulsation, and the long-separation fit is rather unstable. At the same time, at 1064 nm we observe excellent SNR for the BF_i time course, easily resolving the pulsation, including finer features such as the dichrotic notch. These
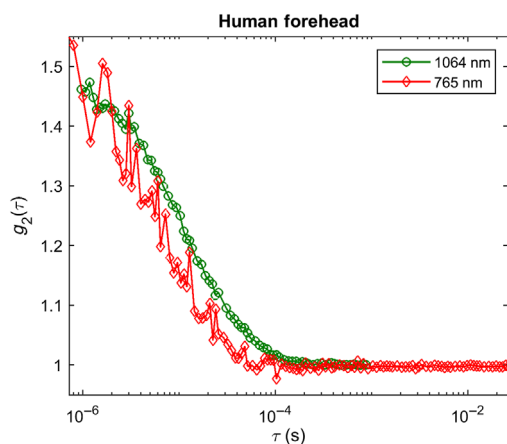
Fig. 8 g_2 measurements at 765 nm (red diamonds) and 1064 nm (green circles) on the forehead of a human subject. The 1064-nm measurements show a later decay and significantly higher SNR.
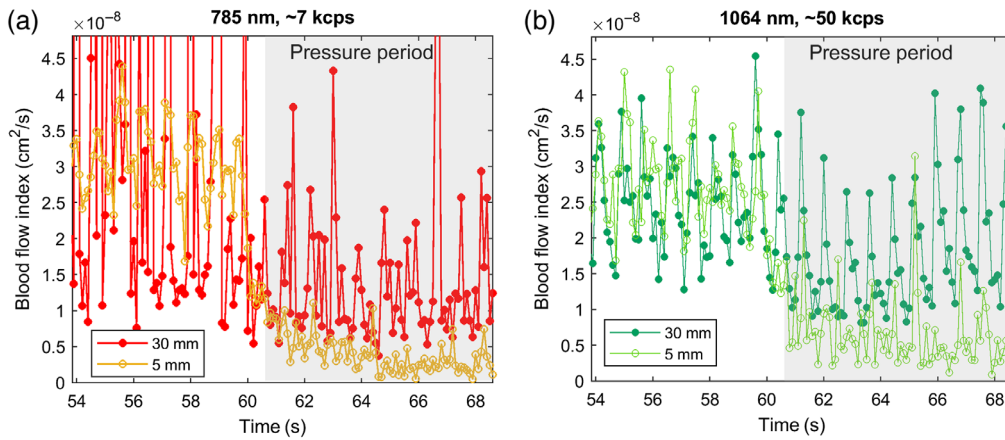
Fig. 9 CW-DCS BF$_i$ time course measurements during pressure modulation maneuvers on the forehead of a human subject using a 10 Hz acquisition rate at (a) 785 nm (orange/red symbols) and (b) 1064 nm (light/dark green symbols), respectively. The short separation (5 mm: orange/light green open circles, respectively) BF$_i$ decreases as expected during the pressure period and is no longer pulsatile; cardiac pulsation remains apparent in the long separation channel (30 mm: red/dark green filled circles, respectively) at both wavelengths; however, only 1064 nm offers sufficient SNR to resolve the pulsation at a 3-cm source–detector separation.

data demonstrate the ability to use 1064 nm DCS as a functional imaging technique with high temporal resolution.

Figure 10 exemplifies TD-DCS measurements in the human forehead at 765 and 1064 nm using a 1-cm source–detector separation and employing the maximum power allowed by the regulatory standards. SNSPDs were used as the detector for both wavelengths. The data were processed at 5 Hz, after which the BF$_i$ values were downsampled to 1/3 Hz to filter out cardiac pulsation and compute the coefficient of variation (CoV). The resulting BF$_i$ CoVs versus gate start time for gates 150 ps wide are shown in Fig. 10(a) for 765 and 1064 nm. Although the CoV increases quicky versus gate at 765 nm and the fit becomes unstable by 600 ps after the peak of the temporal point spread function (TPSF), the 1064-nm curve remains relatively stable until 800 ps after the peak of the TPSF (likely dominated by physiological variability), and the CoV only shows a significant increase at 1 ns after the peak of the TPSF. Figure 10(b) shows the original 5 Hz data for 1064 nm TD-DCS measurements for an early gate (starting at the peak of the TPSF) and a late gate (starting 1 ns after the peak of the TPSF). The BF$_i$ time traces clearly offer sufficient SNR to resolve the cardiac pulsation even at the late gate, exceeding any previously demonstrated TD-DCS measurements with sub 1 s integration times. The achieved SNR
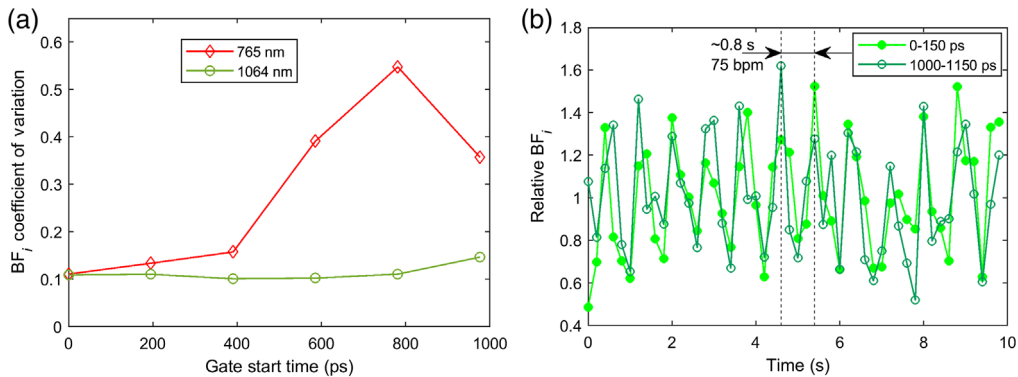
Fig. 10 TD-DCS comparison between 765 and 1064 nm. (a) Comparison of the BF$_i$ CoV versus gate start time for TD-DCS measurements conducted at 765 nm (red diamonds) and 1064 nm (green circles) using a 1-cm source–detector separation and the maximum power allowed by regulatory standards. (b) Evidence of cardiac pulsation in BF$_i$ at a 5-Hz acquisition rate for early (0 to 150 ps, light green filled circles) and late (1000 to 1150 ps, dark green open circles) gates.

highlights the strong potential of TD-DCS as tool for functional brain imaging in addition to neuromonitoring applications.

4 Conclusion

DCS measurements at 1064 nm benefit from a multitude of advantages compared with DCS in the usual NIR range (765 to 850 nm) stemming from lower tissue attenuation, increased amount of light delivery allowed by regulatory standards, reduced energy per photon (enhancing available photon counts), and slower autocorrelation decay moving the transition regime to higher SNR delay time bins. We estimate these advantages through numerical simulations and demonstrate CW-DCS and TD-DCS measurements in phantoms and *in vivo*. These advantages are particularly important for adult brain neuromonitoring applications, for which DCS at 1064 nm can present a dramatic leap forward in performance and is likely to be much more robust, especially in older subjects (where the skin to brain distance may be larger due to brain tissue shrinkage[41]) and those with thicker extracerebral layers. A remaining challenge is the lack of suitable portable photon counting detectors. Potential solutions include developing custom detector designs, using cross-correlation configurations to remove InGaAs SPAD afterpulsing, or employing analog detection in conjunction with a heterodyne DCS approach as done at 850 nm by Zhou et al.[42]

Disclosures

M. A. F. has a financial interest in 149 Medical, Inc., a company developing DCS technology for assessing and monitoring cerebral blood flow in newborn infants, and in Dynometrics, Inc., a company that makes devices that use NIRS technology for athletes to evaluate muscle performance. MAF's interests were reviewed and are managed by Massachusetts General Hospital and Partners HealthCare in accordance with their conflicts of interest policies.

Acknowledgments

Code, Data, and Materials Availability

Data supporting the results reported in the manuscript can be requested by contacting the corresponding author.

References

1. W. Tosh and M. Patteril, "Cerebral oximetry," *BJA Educ.* **16**(12), 417–421 (2016).
2. M. A. Yücel et al., "Functional near infrared spectroscopy: enabling routine functional brain imaging," *Curr. Opin. Biomed. Eng.* **4**, 78–86 (2017).
3. D. A. Boas, L. E. Campbell, and A. G. Yodh, "Scattering and imaging with diffusing temporal field correlations," *Phys. Rev. Lett.* **75**(9), 1855–1858 (1995).

4. D. A. Boas and A. G. Yodh, "Spatially varying dynamical properties of turbid media probed with diffusing temporal light correlation," *J. Opt. Soc. Am. A* **14**(1), 192–215 (1997).

5. E. M. Buckley et al., "Diffuse correlation spectroscopy for measurement of cerebral blood flow: future prospects," *Neurophotonics* **1**(1), 011009 (2014).

6. T. Durduran and A. G. Yodh, "Diffuse correlation spectroscopy for non-invasive, microvascular cerebral blood flow measurement," *Neuroimage* **85**, 51–63 (2014).

7. R. C. Mesquita et al., "Direct measurement of tissue blood flow and metabolism with diffuse optics," *Philos. Trans. R. Soc. A Math. Phys. Eng. Sci.* **369**(1955), 4390–4406 (2011).

8. S. A. Carp et al., "Validation of diffuse correlation spectroscopy measurements of rodent cerebral blood flow with simultaneous arterial spin labeling MRI; towards MRI-optical continuous cerebral metabolic monitoring," *Biomed. Opt. Express* **1**(2), 553–565 (2010).

9. T. Durduran et al., "Optical measurement of cerebral hemodynamics and oxygen metabolism in neonates with congenital heart defects," *J. Biomed. Opt.* **15**(3), 037004 (2010).

10. G. Yu et al., "Validation of diffuse correlation spectroscopy for muscle blood flow with concurrent arterial spin labeled perfusion MRI," *Opt. Express* **15**(3), 1064 (2007).

11. C. Zhou et al., "Diffuse optical monitoring of hemodynamic changes in piglet brain with closed head injury," *J. Biomed. Opt.* **14**(3), 034015 (2009).

12. M. Diop et al., "Calibration of diffuse correlation spectroscopy with a time-resolved near-infrared technique to yield absolute cerebral blood flow measurements: errata," *Biomed. Opt. Express* **3**(6), 1476 (2012)

13. L. He et al., "Noninvasive continuous optical monitoring of absolute cerebral blood flow in critically ill adults," *Neurophotonics* **5**(04), 045006 (2018).

14. V. Jain et al., "Cerebral oxygen metabolism in neonates with congenital heart disease quantified by MRI and optics," *J. Cereb. Blood Flow Metab.* **34**, 380–388 (2014).

15. S. Gunadi et al., "Spatial sensitivity and penetration depth of three cerebral oxygenation monitors," *Biomed. Opt. Express* **5**(9), 2896 (2014).

16. S. Kleiser et al., "Comparison of tissue oximeters on a liquid phantom with adjustable optical properties," *Biomed. Opt. Express* **7**(8), 2973 (2016).

17. E. Okada and D. T. Delpy, "Near-infrared light propagation in an adult head model II Effect of superficial tissue thickness on the sensitivity of the near-infrared spectroscopy signal," *Appl. Opt.* **42**, 2915–2922 (2003).

18. S. N. Davie and H. P. Grocott, "Impact of extracranial contamination on regional cerebral oxygen saturation: a comparison of three cerebral oximetry technologies," *Anesthesiology* **116**, 834–840 (2012).

19. S. K. Samra et al., "Evaluation of a cerebral oximeter as a monitor of cerebral ischemia during carotid endarterectomy," *Anesthesiology* **93**(4), 964–970 (2000).

20. D. Highton, C. Elwell, and M. Smith, "Noninvasive cerebral oximetry: is there light at the end of the tunnel?" *Curr. Opin. Anaesthesiol.* **23**(5), 576–581 (2010).

21. E. Ohmae et al., "Cerebral hemodynamics evaluation by near-infrared time-resolved spectroscopy: correlation with simultaneous positron emission tomography measurements," *Neuroimage* **29**(3), 697–705 2006.

22. J. Selb et al., "Sensitivity of near-infrared spectroscopy and diffuse correlation spectroscopy to brain hemodynamics: simulations and experimental findings during hypercapnia," *Neurophotonics* **1**(1), 015005 (2014).

23. R. H. Wilson et al., "Review of short-wave infrared spectroscopy and imaging methods for biological tissue characterization," *J. Biomed. Opt.* **20**(3), 030901 (2015).

24. D. Kobat, N. G. Horton, and C. Xu, "In vivo two-photon microscopy to 1.6-mm depth in mouse cortex," *J. Biomed. Opt.* **16**(10), 106014 (2011).

25. D. Kobat et al., "Deep tissue multiphoton microscopy using longer wavelength excitation," *Opt. Express* **17**, 13354–13364 (2009).

26. B. Považay et al., "Three-dimensional optical coherence tomography at 1050 nm versus 800 nm in retinal pathologies: enhanced performance and choroidal penetration in cataract patients," *J. Biomed. Opt.* **12**(4), 041211 (2007).

27. P. K. Upputuri and M. Pramanik, "Photoacoustic imaging in the second near-infrared window: a review," *J. Biomed. Opt.* **24**(4), 040901 (2019).

28. S. L. Jacques, "Optical properties of biological tissues: a review," *Phys. Med. Biol.* **58**(11), R37–R61 (2013).
29. S. A. Prahl, "Tabulated molar extinction coefficient for hemoglobin in water," http://omlc.ogi.edu/spectra/hemoglobin/summary.html (2020).
30. N. Bosschaart et al., "A literature review and novel theoretical approach on the optical properties of whole blood," *Lasers Med. Sci.* **29**(2), 453–479 (2014).
31. G. M. Hale and M. R. Querry, "Optical constants of water in the 200-nm to 200-μm wavelength region," *Appl. Opt.* **12**(3), 555 (1973).
32. P. P. Fatouros and A. Marmarou, "Use of magnetic resonance imaging for in vivo measurements of water content in human brain: method and normal values," *J. Neurosurg.* **90**, 109–115 (1999).
33. R. L. P. van Veen et al., "Determination of visible near-IR absorption coefficients of mammalian fat using time- and spatially resolved diffuse reflectance and transmission spectroscopy," *J. Biomed. Opt.* **10**(5), 054004 (2005).
34. N. Baumann and D. Pham-Dinh, "Biology of oligodendrocyte and myelin in the mammalian central nervous system," *Phys. Rev.* **81**(2), 871–927 (2001).
35. C. Zhou, "In-vivo optical imaging and spectroscopy of cerebral hemodynamics," PhD thesis, University of Pennsylvania (2007).
36. T. Durduran et al., "Diffuse optical measurement of blood flow, blood oxygenation, and metabolism in a human brain during sensorimotor cortex activation," *Opt. Lett.* **29**(15), 1766–1768 (2004).
37. L. Gagnon et al., "Double-layer estimation of intra- and extracerebral hemoglobin concentration with a time-resolved system," *J. Biomed. Opt.* **13**(5), 054019 (2008).
38. COTI Lab Northeastern University, "Monte Carlo Extreme (MCX)," http://mcx.space.
39. D. Tamborini et al., "Development and characterization of a multidistance and multiwavelength diffuse correlation spectroscopy system," *Neurophotonics* **5**(1), 011015 (2017).
40. D. Tamborini et al., "Portable system for time-domain diffuse correlation spectroscopy," *IEEE Trans. Biomed. Eng.* **66**(11), 3014–3025 (2019).
41. L. Svennerholm, K. Boström, and B. Jungbjer, "Changes in weight and compositions of major membrane components of human brain during the span of adult human life of Swedes," *Acta Neuropathol.* **94**(4), 345–352 (1997).
42. W. Zhou et al., "Highly parallel, interferometric diffusing wave spectroscopy for monitoring cerebral blood flow dynamics," *Optica* **5**(5), 518 (2018).

Stefan A. Carp received his BS degrees in chemistry and chemical engineering from MIT and his PhD in biomedical optics from the University of California, Irvine, USA. He is an assistant professor of radiology at Harvard Medical School and a member of Massachusetts General Hospital Martinos Center Optics Group. He focuses on the development and clinical translation of innovative techniques for noninvasive tissue hemodynamics and oxygen metabolism monitoring using near-infrared light.

Davide Tamborini received his MSc degree (cum laude) in electronic engineering and his PhD in information and communication technology from the Politecnico di Milano, Milano, Italy, in 2012 and 2015, respectively. He was a research fellow at the Optics Division of the Martinos Center for Biomedical Imaging at Massachusetts General Hospital and Harvard Medical School from 2016 to 2019. He worked on conceiving and developing near-infrared spectroscopy (NIRS) instrumentations for biomedical diagnosis.

Dibbyan Mazumder received his MSc degree in engineering and PhD from the Indian Institute of Science, Bangalore, India. His doctoral thesis is based on quantification of elasticity of tissue/tissue-like materials using vibroacoustography and diffusing wave spectroscopy. Currently, he is a research fellow with Prof. Stefan Carp at the Massachusetts General Hospital Martinos Center Optics Group. His current research focuses on noninvasive cerebral blood monitoring using diffuse correlation spectroscopy.

Oleg Shatrovoy was a member of the technical staff at the MIT Lincoln Laboratory where he contributed to several record-power laser systems, an ultraprecise long-range interferometry

system, a high-data-rate optical communications system, an innovative far-infrared spectroscopy system, and many others. He looks for ways to apply his skills with systems engineering to important problems in biology, physics, and society.

Niyom Lue received his first degree in physical therapy from Mahidol University and his engineering education and master's degree in engineering from Boston University. He continued his PhD education in laser/optics at the University of Massachusetts, while conducting doctoral thesis research at the GR Harrison Spectroscopy Lab of MIT. Currently, he is working as a technical staff at the Laser Technology and Applications Group at Lincoln Laboratory of MIT.

Nisan Ozana is a research fellow at Harvard Medical School, Massachusetts General Hospital and Athinoula A. Martinos Center for Biomedical Imaging. He received his PhD in electrical engineering from Bar Ilan University, Israel in 2019. For his PhD research he received the Wolf Foundation prize and the Prize4Life award. His research interests include neurophotonics, biomedical optics, applied quantum optics, superconductive single photon detectors, super resolution and nanophotonics.

Megan H. Blackwell received her PhD from the Harvard-MIT Division of Health Sciences and Technology. She has been a member of the technical staff at MIT for over a decade and has led efforts developing new electro-optical devices, sensors, and imagers for a range of applications including medical imaging, situational awareness, and remote sensing. She is a member of the technical staff at the Human Health and Performance Systems Group.

Maria A. Franceschini is a professor of radiology at Harvard Medical School with training and expertise in the development of noninvasive optical techniques and applications in neuroscience, neurology, and brain health. As a pioneer in the field of NIRS, she has made substantial contributions to the development of NIRS instruments and to the modeling and testing of diffusion theory to describe light propagation in turbid media. She has successfully applied the technology to numerous functional neuroimaging and clinical neuromonitoring applications.

Biographies of the other authors are not available.